A Polar Scaling Technique for the Regularization of Strongly Singular and Strongly Near-Singular Helmholtz Surface Integrals Evaluated over 2D Domains

Brian J. Vaughn

***Abstract*—The numerical integration of expressions containing strong singularities or strong near-singularities has long been a challenging problem in the electromagnetics community. Much attention has been paid to this problem, as strong $1/R^2$ singularities routinely appear when implementing electromagnetic simulation techniques like the Method of Moments (MoM). To date, several techniques, from singularity extraction to singularity cancellation, have been employed to deal with problems that require the evaluation of 2D strongly-singular integrals. However, no single technique has been proposed that can deal with both strong singularities and strong near-singularities in a fully-numerical manner for arbitrary 2D domains. Moreover, it has been claimed that the Helmholtz-type strongly singular integral found in the MoM is convergent in a principal value sense, but this convergence value has yet to be proven mathematically. In this work, we will conduct the convergence proof and introduce a "polar scaling" change of variables method that may be used to evaluate Helmholtz integrals with both strong and weak singularities/near-singularities. The technique is fully-numerical and can in principle be applied to any planar or curved polygon and any non-singular basis function. We will also provide numerical results showing useful convergence behavior for integrals involving both exact and near-singularities.**

***Index Terms*—Integral Equations, Method of Moments, Numerical Simulation.**

I. Introduction

IT is well known that the method of moments (MoM) technique, a popular method for solving electromagnetic integral equations, requires the numerical evaluation of several integrals containing the Green's function of the inhomogeneous electromagnetic Helmholtz Equation. This Green's function is represented as:

$$G(\vec{x},\, \vec{x}') = \frac{e^{-jkR}}{4\pi R}, \tag{1.1}$$

where k is the wavenumber and

$$R = \sqrt{(x-x')^2 + (y-y')^2 + (z-z')^2}, \tag{1.2}$$

where the primed coordinates denote the position of an electromagnetic current source and the unprimed coordinates denote the observation point. Since the field solution is often desired everywhere within a computational domain, computation for values of R approaching 0 are necessary, leading to the task of evaluating integrals with integrands that contain singularities. One such integral that is often invoked is the following surface integral:

$$\nabla \times \int \vec{\boldsymbol{N}}(\vec{x}') \frac{e^{-jkR}}{4\pi R} dS' = \int \frac{-\vec{R} e^{-jkR}(1+jkR)}{4\pi R^3} \times \vec{\boldsymbol{N}}(\vec{x}')\, dS', \tag{1.3}$$

where $\vec{\boldsymbol{N}}(\vec{x}')$ is a basis function used to approximate a portion of the current source over the surface and $\vec{R}$ is $\vec{x} - \vec{x}'$. Other integrals are involved in the MoM process, but this one is of particular interest, as it contains what is termed a "strong" singularity, i.e., a $1/R^2$ singularity. This type of integral is often treated with the singularity extraction technique, which divides the integral into two, one regular and one singular, and solves the new singular integral analytically [1]-[5]. While powerful and common, this technique is limited in that the analytical integral is not general, and a new formulation must be developed for differing integration domains or basis functions. An equally accurate technique that is more versatile without creating substantially more computational work would therefore have greater utility. Another technique that has been used to treat Helmholtz integral singularities is the singularity cancellation technique, where the integrand is transformed with a change of variables into an expression that no longer contains the singularity, as it is cancelled with the Jacobian [2],[5]-[13]. However, the strong singularity resists cancellation with this method alone and in fact, to the author's knowledge, cancellation schemes have only been achieved for the above

This manuscript has been authored by Fermi Research Alliance, LLC under Contract No. DE-AC02-07CH11359 with the U.S. Department of Energy, Office of Science, Office of High Energy Physics.

B. J. Vaughn is with Fermi National Accelerator Laboratory, Batavia, IL, 60510, USA (e-mail: bvaughn@fnal.gov).

type of integral (with a strong singularity) when it is near-singular, not exactly singular, as the transformations detailed in the works above show diverging or undefined integral limits when the singular point is exactly within the integration source domain. However, several of the near-singularity papers, namely [8] and [9], imply or claim that the exact singularity case is tractable, as the integrand converges to a principal value, and that only the near-singular case is especially challenging. While this principal value claim is true, a proof of the claim for the integral of interest does not appear to have been presented in the literature before now. To be more specific, exactly singular Cauchy Principal Value (CPV) integrals have been investigated in the broader mathematical physics community (e.g., [14]-[15]), but to the author's knowledge, an explicit expression for the principal value of eqn. (1.3) has not been given in the context of the electromagnetic MoM for an arbitrary non-singular basis function, even though the principal value has been claimed to exist. The reference that is often used to support this claim, [7], is a referral to a conference presentation where it is unclear if the claim was proved theoretically, as only the abstract is readily available. It is true that the foundational nature of the work presented in [7] and extensions thereof is not majorly impacted by this missing information. Nevertheless, there appears to be a gap in the development of the theory in this section of the field. This gap will be remedied here. It should be noted that the technique detailed in a recent work, [16], treats both near and exact singularities under the same umbrella by combining singularity extraction with singularity cancellation, but this is subject to the same analytical result limitation as the singularity extraction method alone.

It should also be noted that there exists a class of techniques designed to comprehensibly treat 4D Galerkin integrals commonly found in the MFIE formulation, one of which takes following form:

$$\int_S \overrightarrow{\boldsymbol{N}_m}(\vec{x}) \cdot \int_{S'} \frac{-\vec{R}e^{-jkR}(1+jkR)}{4\pi R^3} \times \overrightarrow{\boldsymbol{N}_n}(\vec{x}')dS'dS\,, \qquad (1.4)$$

where S is an evaluation domain and S' is a source domain [17]-[19]. These methods smoothen the entire 4D kernal by breaking the integral into a sum of contour integrals using non-trivial algebraic manipulations and the Divergence Theorem. On the other hand, the methods discussed thus far, as well as the method presented herein, focus exclusively on accurately evaluating the inner 2D strongly singular integral rather than regularizing the entire 4D kernal. As it happens, and as stated in [17]-[19], a strong motivating element in the development of the 4D-centric summation methods is that accurate evaluation of the inner 2D integral does not imply a smooth 4D kernal and higher accuracy can be achieved for the full 4D integral if it is treated as a whole. However, these methods have not seen popular use as of yet due to the implementation differences between them and existing MoM formulations, as stated in [16]. Because of this, we will proceed with this work focusing exclusively on the strongly singular 2D integral, as its isolated evaluation is still relevant to the community.

Furthermore, the author has identified an opportunity to extend the integration of eqn. (1.3) to polygons with an arbitrary number of edges with one universal standard procedure. A formulation that treats all shapes of this type with the same sequence of variable transformations, regardless of basis function and shape type, presents substantial utility to any platform designed with generality in mind. Using this as a motivation, we will develop a general polar transformation (termed "polar scaling"), mathematically prove that it cancels the strong singularity in the eqn. (1.3) integral, and then connect it to an *N*-sided polygon. We will also detail how the method can be applied to near-singularities, creating a versatile solution for the type of surface integration considered here. The paper will be organized as follows: Section II. will detail the general polar regularization, Section III. will discuss an equally general coordinate renormalization procedure, Section IV. will describe how to complete the polar transformation once a particular shape is chosen, Section V. will discuss near-singularity treatment, and Section VI. will demonstrate a numerical example.

II. Polar Scaling Regularization

As alluded to in Section I, the polar transformation that will be executed below does not cancel the strong singularity in the conventional manner. However, it will be shown that the transformation used here will result in an integrand that is finite at all points within the integration domain, including the strong singularity. That is, the transformed integrand will have a limit that exists as the observation point approaches the source point. We will now formulate this transformation.

Without loss of generality, for a two-dimensional domain described in finite (u, v) coordinates, let us define the following transformation to polar coordinates:

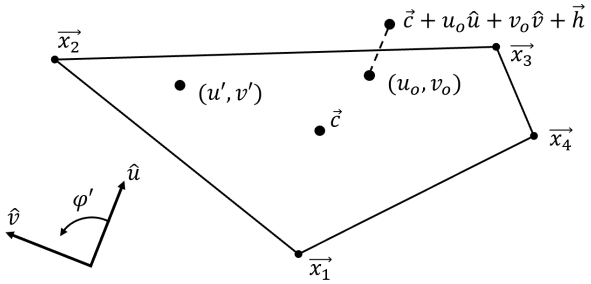

Fig. 1. Arbitrary polygon described in (u, v) coordinate system.

$$u = \rho f(\varphi) + u_0, \qquad (2.1a)$$

$$v = \rho f(\varphi)\tan\varphi + v_0, \qquad (2.1b)$$

with

$$\vec{x} = \vec{c} + u\hat{u} + v\hat{v} + \vec{h}, \qquad (2.1c)$$

$$\vec{x}' = \vec{c} + u'\hat{u} + v'\hat{v}\,, \qquad (2.1d)$$

where $f(\varphi)$ is some continuous angular function with $|f(\varphi)|, |f(\varphi)\tan\varphi| < \infty$ for all φ, $\vec{c}$ is the source domain centroid, $\hat{u}$ and $\hat{v}$ are orthogonal, but otherwise arbitrary normal vectors, and (u_0, v_0) is the position of the observation point if it

is within the source domain, or the projection of the observation point onto the source domain if the observation point is not within the source domain. $\vec{h}$ applies to the case where the observation point is not within the source domain and represents the vector between the observation point and its source domain projection ($\vec{h}$ is merely the 0 vector if the observation point lies within the source domain). $|\vec{h}|$ is the shortest distance between the observation point and any point in the source domain. Note that ρ is real and $0 \le \rho \le 1$. $\hat{u}$ and $\hat{v}$ potential definitions will be discussed in Section IV. Fig. 1 illustrates this coordinate system, but ρ is omitted as its calculation will also be discussed in Section IV; we do not need its mathematical definition to show regularization as will become clear below. The Jacobian for the change of variables from the (u, v) domain to the (ρ, φ) domain is

$$\left|J_{\rho\varphi}\right| = \rho f(\varphi)^2 \sec^2 \varphi. \tag{2.2}$$

We may substitute these transformations into our expression for R, resulting in the following:

$$R = \sqrt{\sum_n^{x,y,z} \begin{Bmatrix} \widehat{u_n}\left(\rho f(\varphi) - \rho' f(\varphi')\right) \\ +\widehat{v_n}(\rho f(\varphi)\tan\varphi - \rho' f(\varphi')\tan\varphi') + h\widehat{h_n} \end{Bmatrix}^2}. \tag{2.3}$$

We stipulate that (u_0, v_0) is the transformed observation point or projection, so ρ is 0. As such, eqn. (2.3) becomes

$$R = \sqrt{\sum_n^{x,y,z} \left(\widehat{u_n}\rho' f(\varphi') + \widehat{v_n}\,\rho' f(\varphi')\tan\varphi' - h\widehat{h_n}\right)^2}, \tag{2.4}$$

where $h = |\vec{h}|$ and $\hat{h}$ is the unit vector in the direction of $\vec{h}$. Note that we factored out -1 to reorient the signs in the expression. Let us now use the transformations executed thus far to manipulate the strongly singular Helmholtz integral described in eqn. (1.3):

$$\begin{aligned} &\int \frac{-\vec{R}e^{-jkR}(1+jkR)}{4\pi R^3} \times \vec{\boldsymbol{N}}(\vec{x}')\, dS' \\ &\quad = \int \frac{-e^{-jkR}(1+jkR)}{4\pi R^3} \\ &\quad * \begin{Bmatrix} (x-x')\left(N_y(\vec{x}')\hat{z} - N_z(\vec{x}')\hat{y}\right) \\ +(y-y')(N_z(\vec{x}')\hat{x} - N_x(\vec{x}')\hat{z}) \\ +(z-z')\left(N_x(\vec{x}')\hat{y} - N_y(\vec{x}')\hat{x}\right) \end{Bmatrix} dS' \end{aligned} \tag{2.5}$$

Let us consider only the first term in the brackets for now, leading to the following integral:

$$\begin{aligned} &\int \frac{-e^{-jkR}(1+jkR)}{4\pi R^3}\{(x-x')\left(N_y(\vec{x}')\hat{z}\right. \\ &\quad \left. - N_z(\vec{x}')\hat{y}\right)\}dS' \end{aligned} \tag{2.6}$$

Further, let

$$N_{yz} \equiv \left(N_y(\vec{x}')\hat{z} - N_z(\vec{x}')\hat{y}\right) \tag{2.7}$$

Substituting the coordinate transformations into eqn. (2.6), we obtain

$$\begin{aligned} &\int \frac{-e^{-jkR}(1+jkR)}{4\pi R^3}\{(x-x')\left(N_y(\vec{x}')\hat{z} - N_z(\vec{x}')\hat{y}\right)\}dS' \\ &= \int\int \frac{-e^{-jkR}(1+jkR)}{4\pi R^3}\{[\widehat{u_x}(u-u') + \widehat{v_x}(v-v') + h\widehat{h_x}] \\ &\quad * N_{yz}(\rho', \varphi')\}\left|J_{\rho'\varphi'}\right| d\rho' d\varphi' \\ &= \int\int \frac{e^{-jkR}(1+jkR)}{4\pi R^3} \\ &\quad * \{\left[\widehat{u_x}\rho' f(\varphi') + \widehat{v_x}\rho' f(\varphi')\tan\varphi' - h\widehat{h_x}\right] N_{yz}(\rho', \varphi')\} \\ &\quad * \rho' f(\varphi')^2 \sec^2\varphi'\, d\rho' d\varphi' \end{aligned} \tag{2.8}$$

Note that the negative sign in front of the exponential was absorbed into the expression in the square brackets. Also note that the ρ' bounds are 0 and 1, whereas the φ' bounds are 0 and 2π. These details will be more closely described later on when we specify the computation of ρ and $f(\varphi)$. Substituting eqn. (2.4) into eqn. (2.8) and splitting the expression into two integrals, we arrive at the following result:

$$\begin{aligned} &\int\int \frac{e^{-jk\sqrt{\sum_n^{x,y,z}\left(\widehat{u_n}\rho' f(\varphi') + \widehat{v_n}\,\rho' f(\varphi')\tan\varphi' - h\widehat{h_n}\right)^2}}}{4\pi\left[\sqrt{\sum_n^{x,y,z}\left(\widehat{u_n}\rho' f(\varphi') + \widehat{v_n}\,\rho' f(\varphi')\tan\varphi' - h\widehat{h_n}\right)^2}\right]^3} \\ &\quad * \begin{bmatrix} \widehat{u_x}\rho' f(\varphi') \\ +\widehat{v_x}\,\rho' f(\varphi')\tan\varphi' \\ -h\widehat{h_x} \end{bmatrix} N_{yz}(\rho', \varphi')\rho' f(\varphi)^2 \sec^2\varphi'\, d\rho' d\varphi' \\ &\quad + \int\int \frac{jke^{-jk\sqrt{\sum_n^{x,y,z}\left(\widehat{u_n}\rho' f(\varphi') + \widehat{v_n}\,\rho' f(\varphi')\tan\varphi' - h\widehat{h_n}\right)^2}}}{4\pi\sum_n^{x,y,z}\left(\widehat{u_n}\rho' f(\varphi') + \widehat{v_n}\,\rho' f(\varphi')\tan\varphi' - h\widehat{h_n}\right)^2} \\ &\quad * \begin{bmatrix} \widehat{u_x}\rho' f(\varphi') \\ +\widehat{v_x}\,\rho' f(\varphi')\tan\varphi' \\ -h\widehat{h_x} \end{bmatrix} N_{yz}(\rho', \varphi')\rho' f(\varphi')^2 \sec^2\varphi'\, d\rho' d\varphi' \end{aligned} \tag{2.9}$$

Since the second integral in eqn. (2.9) was weakly singular in its original form, its singularity is cancelled by the polar transformation for $h = 0$ (ρ' terms cancel under this circumstance). Note that since $f(\varphi')$, as a stipulation of the transformation, is defined in such a way that $|f(\varphi')\tan\varphi'| < \infty$, $|f(\varphi')\sec\varphi'| < \infty$ as well, so the integrand of the second integral cannot have a φ' singularity associated with it for a non-

singular $N_{yz}(\rho',\varphi')$. The numerical stability of this integral, then, is dependent on the variational stability of $f(\varphi')$, which, as we will define in Section IV, is dependent on the polygon shape. The focus of this work is on management of the $1/R^2$ strong singularity displayed in eqn. (1.3), so an exhaustive analysis of the stability of this ancillary integral is beyond the scope of this paper. However, this angular integrand will be shown in Section VI to be well-behaved for the examples discussed therein, which are representative of typical scenarios found in electromagnetic MoM problems. As such, the second integral may be evaluated numerically using standard quadrature rules such as the well-known Gauss-Legendre method.

The first integral, in fact, is also convergent despite the integrand's $\rho'=0, h=0$ singularity, but the justification of this claim is more involved. To show that the first integral is regular, we will examine its behavior as $\rho'\to 0$ for $h=0$ (the observation point is in the source domain). When $h=0$, the first eqn. (2.9) integral simplifies to the following expression:

$$\int \frac{\int I_x(\rho',\varphi')\,d\varphi'}{4\pi\rho'}d\rho', \tag{2.10}$$

with

$$I_x(\rho',\varphi') \equiv \operatorname{sgn}(\cos\varphi')\frac{e^{-jk\rho' f(\varphi')\sqrt{\sum_n^{x,y,z}(\widehat{u_n}+\widehat{v_n}\tan\varphi')^2}}}{\left[\sum_n^{x,y,z}(\widehat{u_n}+\widehat{v_n}\tan\varphi')^2\right]^{\frac{3}{2}}}$$

$$*\left\{\left[\widehat{u_x}+\widehat{v_x}\tan\varphi'\right]N_{yz}(\rho',\varphi')\right\}\sec^2\varphi'. \tag{2.11}$$

Note that the cancellations from the simplification yield an expression that includes $\operatorname{sgn}(f(\varphi'))$. Here, we have replaced the signum argument with $\cos\varphi'$ since $\operatorname{sgn}(\cos\varphi')$ and $\operatorname{sgn}(f(\varphi'))$ are equal. This is apparent by consulting Fig. 1. When $-\frac{\pi}{2}<\varphi'<\frac{\pi}{2}$, $u'>u_0$, so $\operatorname{sgn}\big(f(\varphi')\big)$ must be positive. The opposite is true when $\frac{\pi}{2}<\varphi'<\frac{3\pi}{2}$.

From here, we wish to take the limit of eqn. (2.11) as $\rho'\to 0$, where the integrand appears to diverge. If the limit exists, however, the integral is regular. To prove that the limit is indeed finite, we notice that if $\lim_{\rho'\to 0}\int I(\rho',\varphi')\,d\varphi'=0$, the ρ' integrand in eqn. (2.10) is a L'Hopital indeterminant. When $\rho'=0$, $I_x(\rho',\varphi')$ becomes

$$I_x(0,\varphi') = \frac{\operatorname{sgn}(\cos\varphi')}{\left[\sum_n^{x,y,z}(\widehat{u_n}+\widehat{v_n}\tan\varphi')^2\right]^{\frac{3}{2}}}$$

$$*\left[\widehat{u_x}+\widehat{v_x}\tan\varphi'\right]N_{yz}(0,\varphi')\sec^2\varphi'. \tag{2.12}$$

Note that when $\rho'=0$, N_{yz} is no longer a function of φ'. We now represent the numerator integral of eqn. (2.11), in a principal value sense, as follows:

$$\int_0^{2\pi} I_x(0,\varphi')d\varphi'$$

$$=\lim_{\epsilon\to 0}\int_{-\frac{\pi}{2}+\epsilon}^{\frac{\pi}{2}-\epsilon} I_x(0,\varphi')d\varphi' + \int_{\frac{\pi}{2}+\epsilon}^{\frac{3\pi}{2}-\epsilon} I_x(0,\varphi')d\varphi'. \tag{2.13}$$

The bounds are chosen to coincide with the divergent points in the tangent and secant functions in the integrand. Using the same tangent-secant limit arguments as those used for the second integral of eqn. (2.9), we see that $I(0,\varphi')$ does not diverge at the integral bounds as $\epsilon\to 0$. Also note that for the first integral in eqn. (2.13), $\operatorname{sgn}(\cos\varphi')=1$, whereas $\operatorname{sgn}(\cos\varphi')=-1$ in the second integral. We also notice that for $\varphi'\neq\frac{p\pi}{2}$ for some odd integer p,

$$\tan(\varphi'+\pi)=\tan\varphi', \tag{2.14a}$$

$$\sec^2(\varphi'+\pi)=\sec^2\varphi'. \tag{2.14b}$$

Since the intervals of the two integrals in eqn. (2.13) are offset by π, it is clear that

$$\left|\lim_{\epsilon\to 0}\int_{-\frac{\pi}{2}+\epsilon}^{\frac{\pi}{2}-\epsilon} I_x(0,\varphi')d\varphi'\right| = \left|\lim_{\epsilon\to 0}\int_{\frac{\pi}{2}+\epsilon}^{\frac{3\pi}{2}-\epsilon} I_x(0,\varphi')d\varphi'\right|. \tag{2.15}$$

Therefore,

$$\lim_{\epsilon\to 0}\int_{-\frac{\pi}{2}+\epsilon}^{\frac{\pi}{2}-\epsilon} I_x(0,\varphi')d\varphi' + \int_{\frac{\pi}{2}+\epsilon}^{\frac{3\pi}{2}-\epsilon} I_x(0,\varphi')d\varphi'$$

$$=\lim_{\epsilon\to 0}\int_{-\frac{\pi}{2}+\epsilon}^{\frac{\pi}{2}-\epsilon} I_x(0,\varphi')d\varphi' - \int_{-\frac{\pi}{2}+\epsilon}^{\frac{\pi}{2}-\epsilon} I_x(0,\varphi')d\varphi' = 0. \tag{2.16}$$

The limit in eqn. (2.10), then, is indeed a L'Hopital indeterminant, and thus may be evaluated via L'Hopital's rule. Differentiating the numerator and denominator of eqn. (2.10) with respect to ρ', we can take the limit of eqn. (2.10) as follows:

$$\lim_{\rho'\to 0}\frac{\int I_x(\rho',\varphi')\,d\varphi'}{4\pi\rho'}$$

$$=\frac{1}{4\pi}\int -jkf(\varphi')\sqrt{\sum_n^{x,y,z}(\widehat{u_n}+\widehat{v_n}\tan\varphi')^2}\;I_x(0,\varphi')d\varphi', \tag{2.17}$$

In which the $\rho'=0$ singularity has been eliminated. This analysis shows that the polar mapping defined in eqn. (2.1) reveals that the strong singularity of the Helmholtz integral is a "false" singularity, one that does not truly cause the integrand ρ'

to diverge. As such, both integrals of eqn. (2.9) may be evaluated numerically, using conventional quadrature rules without the need for singularity extraction. In fact, examining eqn. (2.9), we find that the limit integral in eqn. (2.17), when $\rho' = 0$, is *exactly equal* to the second φ' integral in eqn. (2.9) in magnitude and opposite in sign. This means that at the $\rho' = 0$ point, the total integrand is null, i.e., *the* $\rho' = 0$ *point contributes nothing to the integral*. This is also trivially true if $\rho' = 0$ and $h \neq 0$. Identical arguments may be made to evaluate the second and third terms of eqn. (2.5). Note that the transformation described in this section is applicable to any 2D shape. This is a powerful result since, as far as 2D shapes are concerned, it allows for a technique that can handle both exact and near strong singularities with the same transformation, simplifying code implementations. It should be noted that weakly singular $1/R$ Helmholtz integrals also have their singularities cancelled with this transformation, much like the second integral in eqn. (2.9). This means that the formulation is also open to problems involving $1/R$ potential integrals. In the next section, we will explain the method of moving the polygon definition to the (u, v) space.

III. (u, v) Transformation

Consider a polygon defined in Cartesian space by N arbitrary points $\overrightarrow{x_1}$, $\overrightarrow{x_2}$, … and $\overrightarrow{x_n}$ defined as

$$\overrightarrow{x_n} = \left(x_{nx},\ x_{ny},\ x_{nz}\right),\ n = 1, 2, \dots N. \tag{3.1}$$

We will execute an unscaled change of basis to represent the points within the polygon in terms of two orthogonal vectors that are in-plane with the polygon surface. The exact choice of basis is somewhat arbitrary, and many definitions are available. Here, we will choose the unit vector pointing from the polygon centroid $\vec{c}$ to the vertex $\overrightarrow{x_2}$ as our first basis vector, which will establish the $\hat{v}$ direction (note, as shown in Fig. 1, the convention for this work is to label the lower left vertex of the polygon as $\overrightarrow{x_1}$ and increase the vertex numbering in the clockwise direction). $\vec{c}$ may be easily computed as

$$\vec{c} = \frac{1}{N}\begin{bmatrix} \sum_{n=1}^{N} x_{nx}\,, \\ \sum_{n=1}^{N} x_{ny}\,, \\ \sum_{n=1}^{N} x_{nz} \end{bmatrix}. \tag{3.2}$$

With this convention, $\hat{v}$ may be explicitly computed as

$$\hat{v} = \frac{\overrightarrow{x_2} - \vec{c}}{|\overrightarrow{x_2} - \vec{c}|}. \tag{3.3}$$

Using the unit vector pointing from $\overrightarrow{x_1}$ to $\overrightarrow{x_2}$, which we will label as $\widehat{l_{21}}$, we may develop an orthogonal vector to $\hat{v}$, which we will term $\hat{u}$:

$$\hat{u} = \frac{\hat{v} \times \widehat{l_{21}} \times \hat{v}}{\left|\hat{v} \times \widehat{l_{21}} \times \hat{v}\right|} = \frac{\widehat{l_{21}} - \hat{v}\left(\hat{v} \cdot \widehat{l_{21}}\right)}{\left|\widehat{l_{21}} - \hat{v}\left(\hat{v} \cdot \widehat{l_{21}}\right)\right|}, \tag{3.4}$$

where the BAC-CAB vector triple product identity has been used. Note that any in-plane vector that is not parallel to $\hat{v}$ may be used in place of $\widehat{l_{21}}$ and the resulting vector will be the same after normalization. We now represent each point within the polygon via the following function:

$$\vec{x}' = \vec{c} + u'\hat{u} + v'\hat{v}, \tag{3.5}$$

where u' and v' are constants. To find the constants that correspond to the point of interest $\overrightarrow{x'}$, we use individual components of eqn. (2.5) to create a system of equations, which may be represented in matrix form as below:

$$\begin{bmatrix} \widehat{u_x} & \widehat{v_x} \\ \widehat{u_y} & \widehat{v_y} \end{bmatrix}\begin{bmatrix} u' \\ v' \end{bmatrix} = \begin{bmatrix} (\vec{x}' - \vec{c})_x \\ (\vec{x}' - \vec{c})_y \end{bmatrix}. \tag{3.6}$$

Solving this matrix equation yields the unknown constants. Note that since all the points in the polygon are coplanar, each pair of two components can only correspond to one potential third coordinate while remaining in-plane, so only two of the components of eqn. (3.4) need to be invoked to find the unknown constants (here the x and y components are used). Note also that our differential element dS' is now $du'dv'$. Since the Euclidean distances between points in our new basis and the original Cartesian basis are identical, no scaling factors are needed to execute the change of variables. We are now prepared to execute the polar mapping for polygons. This will be done in the next section.

IV. Polygon Polar Coordinates

Here, we will demonstrate an example of how to execute the polar mapping described in the previous sections for arbitrary polygons with straight edges. Note that as long as the edges are straight, the following procedure will be the same regardless of whether or not the polygon has concave or convex sections. The polar coordinates ρ' and φ' are defined in relation to the point (u_0, v_0) and the polygon vertices. From Fig. 1, it is clear that φ' is defined by the direction of the vector pointing from (u_0, v_0) to (u', v'). ρ', in our formulation, will refer to an inner polygon scaling factor that corresponds to the dimensions of a similar polygon to the polygon under consideration (note that the term "similar" is meant in the mathematical geometric sense). This similar polygon will be termed the "scaled" polygon. The scaled polygon has an edge that intersects with (u', v') and vertices that lie on the lines drawn between (u_0, v_0) and the vertices of the larger polygon, which we will term the "base" polygon. Fig. 2 illustrates this scaling concept. When $\rho' = 1$, (u', v') lies on the base polygon boundary. Note that this representation of ρ' is quite similar to the formulation of the y' variable discussed in [20], though the second variable used in that work, x', is linear instead of the polar variable φ' used here, which, again, is necessary for the strong singularity cancellation proof discussed herein. We now define vertex vectors:

$$\overrightarrow{w_n} = \overrightarrow{p_n} - (u_0, v_0), \quad n = 1, 2, \dots N. \tag{4.1}$$

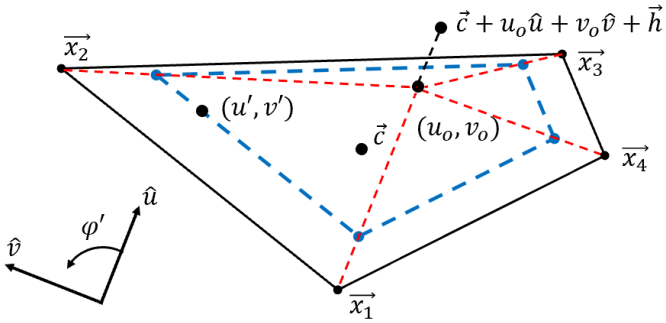

Fig. 2. Polygon scaling. The black polygon is the base polygon and the dashed blue polygon is the scaled polygon. The scaled polygon vertices lie on the red dashed lines connecting (u_0, v_0) to the base polygon vertices and the scaled polygon edges are parallel to the base polygon edges. (u', v') lies on a scaled polygon edge and ρ' is determined by how large the scaled polygon must be for its boundary to intersect with (u', v').

where $\overrightarrow{p_n}$ denotes the (u, v) coordinates of vertex n. These vectors will be used to determine the scaling of the similar polygon, and thus, ρ'. For some (u', v') that we wish to map, we first must determine which edge the similar polygon will intersect the point with. We may do this by simply computing φ' via

$$\varphi' = \tan^{-1}\frac{v'-v_0}{u'-u_0}. \tag{4.2}$$

We also define vertex φ' values as

$$\varphi'_n = \tan^{-1}\frac{w_{nv}}{w_{nu}}, \qquad n = 1, 2, \dots N. \tag{4.3}$$

where w_{np} denotes the p-component of $\overrightarrow{w_n}$. If $\varphi'_{n+1} \le \varphi' < \varphi'_n$ the point is on edge $e_{(n+1)n}$. We will term the edge that corresponds to the φ' value as the "active" edge. Note that if (u_0, v_0) lies on a vertex, one of the vertex vectors will be 0 and its inverse tangent computation will be undefined. If φ' is within an interval with an undefined bound, this undefined bound is replaced by the next defined bound in the sequence counting down from N to 1 and circling back to N. For example, for $N = 3$, if the undefined bound is φ'_3, we set $\varphi'_3 = \varphi'_2$ instead. If the undefined bound is φ'_2, we set $\varphi'_2 = \varphi'_1$. Finally, if the undefined bound is φ'_1, we set $\varphi'_1 = \varphi'_3$. This effectively merges two potential active edges together. As we will see below, both of the merged active edges are treated identically regarding the numerical integration operation. Once the active edge is known, we may use the vertex vectors to determine the intersection.

For a straight edge e_{ij}, let

$$(u', v') = (u_0, v_0) + \rho'\overrightarrow{w_j} + \beta\rho'\left(\overrightarrow{w_i} - \overrightarrow{w_j}\right), \tag{4.4}$$

and let

$$\overrightarrow{w_{ij}} = \overrightarrow{w_i} - \overrightarrow{w_j} = \overrightarrow{p_i} - \overrightarrow{p_j}, \tag{4.5}$$

where β is some constant. Note that the i-j indexing assumes clockwise vertex increment, so starting at vertex 1 for $N = 3$, the edges are e_{21}, e_{32}, and e_{13}. Qualitatively, this operation shifts the observation point to the j[th] vertex of the scaled polygon that intersects with the source point and then moves along e_{ij} of the scaled polygon until the source point is reached. This gives us two equations, one composed of u coordinates and one composed of v coordinates. By substitution, it is straightforward to eliminate β and show that

$$\rho' = \frac{w_{iju}(v'-v_0) - w_{ijv}(u'-u_0)}{w_{jv}w_{iju} - w_{ju}w_{ijv}}, \tag{4.6}$$

where the u and v subscripts denote the u and v components of the vectors. Note that when $\rho' = 1$, the source point always lies on the polygon perimeter. Using eqn. (4.2), we may represent u' in terms of ρ' as

$$u' = \rho'\frac{w_{jv}w_{iju} - w_{ju}w_{ijv}}{w_{iju}\tan\varphi' - w_{ijv}} + u_0. \tag{4.7}$$

From our definition in eqn. (2.1), this implies the azimuth function $f(\varphi')$ is

$$f(\varphi') = \frac{w_{jv}w_{iju} - w_{ju}w_{ijv}}{w_{iju}\tan\varphi' - w_{ijv}}. \tag{4.8}$$

This function encodes the varying Euclidean distance between (u_0, v_0) and the source point as the scaled polygon edge is traversed, allowing for the transformation to be standardized across all polygon shapes under a single formulation. While we are effectively breaking the polygon into N sub-triangles, similarly to other polar formulations, it is the consideration of each scaled polygon as its own unified shape with constant "radius" ρ' that differentiates the proposed scheme. This thinking ultimately facilitates 0 to 2π angular extent crucial to the proof of convergent exact strong singularity presented in the previous section. As we will see in Section VI, the azimuth function combined with the rest of the integrands of the polar scaling formulation exhibit an angular dependence that is smooth enough to be tractable using Gaussian quadrature rules for the φ' integration. The number of necessary sample points will be discussed in Section VI. We also see that the function $f(\varphi')$ defined in this way is indeed bounded for all φ'. To understand why, we consider whether or not the denominator of eq. (4.8), $w_{iju}\tan\varphi' - w_{ijv}$, can ever be 0. The first way this could happen is if both w_{iju} and w_{ijv} could be zero at the same time, but this is a trivial case where the active edge has a length of 0 and thus would not contribute to the integration or polygon definition. The second way the denominator could be zero is if $\tan\varphi' = w_{ijv}/w_{iju}$ for some φ' between φ'_i and φ'_j as defined by eqn. (4.3). However, for a polygon interior/exterior (u_0, v_0), this is not possible for the values of φ' defined by the edge vertices, as, if $\tan\varphi' = w_{ijv}/w_{iju}$, then the vector pointing from (u_0, v_0) to the point on the active edge would have to be parallel to the active edge itself. This is only possible if (u_0, v_0) lies on an edge or vertex, which are special cases that will be discussed

in the following paragraph.

If (u_0, v_0) lies on an edge or vertex of the base polygon and φ' is such that the active edge of the scaled polygon overlaps entirely with the base polygon boundary, $w_{jv}w_{iju} = w_{ju}w_{ijv}$ for all φ' in that interval, and thus, $(u', v') = (u_0, v_0)$ since $f(\varphi') = 0$ nominaly. To show that this is the case, consider (u_0, v_0) lying on an arbitrary edge/vertex. Again, if this is the case, then every point on one or two of the scaled polygon edges overlaps with the base polygon boundary (one if the source point is on a base polygon edge and not a vertex, and two if it's on a vertex). Let e_{ijb} be the base polygon edge that overlaps with one of the scaled polygon edges. Given the overlap, it is clear that $\overrightarrow{e_{ijb}} \times \overrightarrow{w_i} = \overrightarrow{e_{ijb}} \times \overrightarrow{w_j} = 0$ (note $\overrightarrow{e_{ijb}}$ is the vector between vertex i and vertex j). Therefore, we may state that for some constant α, $\overrightarrow{w_i} = \alpha\overrightarrow{w_j}$, meaning that $\overrightarrow{w_{ij}} = (\alpha - 1)\overrightarrow{w_j}$. Since $(\alpha - 1)$ is scalar, it is clear then that $w_{jv}w_{iju} = w_{ju}w_{ijv}$ for this case. However, ρ' is not necessarily equal to 0, depending on the size of the scaled polygon under consideration. Note that eqn. (4.6) cannot be used in this case to determine ρ' since direct evaluation yields an indeterminant. Since our objective is numerical integration, however, we may simply assert ρ' values during the evaluation process, so the potential ambiguity is not a problem. This leads us back to the case where $\tan\varphi' = w_{ijv}/w_{iju}$, which is made moot by the fact that the numerator of eqn. (4.8) is 0 on the active edge if (u_0, v_0) lies on an edge or vertex. Technically, the evaluation of eqn. (4.8) at the upper bound of φ' for such an active edge yields a 0/0 indeterminant. However, we may assert that the function $f(\varphi')$ be continuous within the bounds of an active edge without affecting the end result of the integration since this indeterminacy only occurs at single points that, alone, give infinitesimally small contributions. As such, $f(\varphi')$ is bounded under our definitions.

In any case, a $f(\varphi')$ equal to 0 does not change the analysis (it merely causes the integrand exponential and the $\rho' = 0$ limit integrand to vanish), and thus, edge/vertex observation points do not require special treatment other than the active edge merging described above if the observation point is a vertex.

In the next section, we will extend the above formulation to curvilinear shapes.

V. Curvilinear Extension

We now consider an M^{th}-order curvilinear polygon defined by N*M nodes, where N is the number of polygon vertices. In order to treat this polygon with the polar scaling technique, we first need to map its surface to that of a planar polygon. The planar polygon we will choose will be the one created by the curvilinear polygon's vertices connected by straight edges. Further, we will define the planar polygon in (u', v') space so that we may apply the polar transformation immediately after the initial mapping.

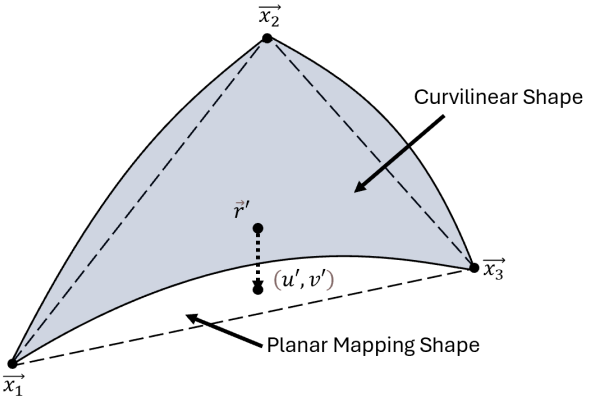

Fig. 3. Scheme for mapping curvilinear shape to planar version so polar scaling may be applied.

This mapping choice is illustrated in Fig. 3. Let $\vec{r}'$ be some point on the curvilinear polygon in Cartesian space. With this in mind, we define the following polynomial mapping function:

$$\vec{r}' = \sum_{i=0}^{M}\sum_{j=0}^{i} \overrightarrow{b_{ij}}(u' - u_0)^{i-j}(v' - v_0)^j, \tag{5.1}$$

where $\overrightarrow{b_{ij}}$ are vector-valued expansion coefficients and u, v are defined on the planar polygon as per Section III. The nodes on the curvilinear polygon are mapped to known locations on the planar version. For example, in the case of an $M = 2$ (quadratic) triangular curvilinear shape, the definition nodes would be placed at the polygon vertices as well as the midpoints of the polygon edges, 6 points in total. On the planar polygon, these nodes would still map to the planar shape vertices and edge midpoints. Since every point has 3 vector components, we have 18 equations and 18 unknowns (each of the 6 unknown vector coefficients has 3 components as well). This system of equations may be easily solved with well-known matrix techniques. A similar procedure applies to any value of M.

Once the coefficients are known, we may compute the Jacobian for the transformation from the curvilinear polygon to the planar version. For each point $\vec{r}'$ on the curvilinear polygon surface, we define a local differential surface element $d\alpha d\beta$, where α and β are local area coordinates each with their own associated orthogonal unit vectors $\hat{\alpha}$ and $\hat{\beta}$, which are tangent to the curvilinear polygon surface at each $\overrightarrow{r'}$. Then, the Jacobian would be evaluated as

$$J_c(u', v') = \begin{vmatrix} \frac{\partial\alpha}{\partial u'} & \frac{\partial\alpha}{\partial v'} \\ \frac{\partial\beta}{\partial u'} & \frac{\partial\beta}{\partial v'} \end{vmatrix}. \tag{5.2}$$

Since $\hat{\alpha}$ and $\hat{\beta}$ need only be orthogonal and tangent to the polygon surface and are otherwise arbitrary, we may utilize the orthogonality of the (u', v') space formulation. Namely, we may define $\hat{\alpha}$ as the unit vector pointing in the direction of $\frac{\partial\vec{r}}{\partial u'}$ and $\hat{\beta}$ as the unit vector pointing in the direction of $\frac{\partial\vec{r}}{\partial v'}$. Then we may

represent the local differentials $d\alpha$ and $d\beta$ as follows:

$$d\alpha = \left|\frac{\partial \vec{r}}{\partial u'}\right| du', \tag{5.3a}$$

$$d\beta = \left|\frac{\partial \vec{r}}{\partial v'}\right| dv', \tag{5.3b}$$

which immediately give $\frac{\partial \alpha}{\partial u'}$ and $\frac{\partial \beta}{\partial v'}$. Note that with this definition, $\frac{\partial \alpha}{\partial v'} = \frac{\partial \beta}{\partial u'} = 0$ due to the orthogonality of $\hat{u}$ and $\hat{v}$ (as such, the total and partial derivatives are equal). Therefore,

$$J_c(u', v') = \left|\frac{\partial \vec{r}'}{\partial u'}\right| \left|\frac{\partial \vec{r}'}{\partial v'}\right|$$

$$= \left|\sum_{i=0}^{M}\sum_{j=0}^{i}(i-j)\overrightarrow{b_{ij}}(u'-u_0)^{i-j-1}(v'-v_0)^{j}\right| * \left|\sum_{i=0}^{M}\sum_{j=0}^{i}(j)\overrightarrow{b_{ij}}(u'-u_0)^{i-j}(v'-v_0)^{j-1}\right|. \tag{5.4}$$

With this mapping, we may now execute the polar scaling transformation on the planar polygon. Doing this, R from eqn. 1.3 and the curvilinear mapping Jacobian become

$$R = \sqrt{\sum_{n}^{x,y,z}\left(\sum_{i=0}^{M}\sum_{j=0}^{i}\left[\overrightarrow{b_{ijn}}\left(\rho' f(\varphi')\right)^{i-j}(\rho' f(\varphi')\tan\varphi')^{j}\right] - \overrightarrow{b_{00n}} - h\widehat{h_n}\right)^2}, \tag{5.5}$$

$$J_c(\rho', \varphi') = \left|\sum_{i=0}^{M}\sum_{j=0}^{i}(i-j)\overrightarrow{b_{ij}}(\rho' f(\varphi'))^{i-j-1}(\rho' f(\varphi')\tan\varphi')^{j}\right| * \left|\sum_{i=0}^{M}\sum_{j=0}^{i}(j)\overrightarrow{b_{ij}}\left(\rho' f(\varphi')\right)^{i-j}(\rho' f(\varphi')\tan\varphi')^{j-1}\right|. \tag{5.6}$$

where $\overrightarrow{b_{ijn}}$ is the n-component of the ij vector coefficient and $h\widehat{h_n}$ has the same definition as in Section II. Note that $\overrightarrow{b_{00n}}$ is subtracted in eqn. (5.5) since, when $i = j = 0$, $\vec{r}$ is not 0, but $\overrightarrow{b_{00x}}\hat{x} + \overrightarrow{b_{00y}}\hat{y} + \overrightarrow{b_{00z}}\hat{z}$ since $0^0 = 1$. These expressions may be readily substituted into eqn. (2.5) to obtain equations analogous to eqn. (2.9).

Of course, the question now arises whether the regularization shown in Section II persists under the curvilinear transformation now that the integrand contains higher-order polynomials in ρ'. In fact, the arguments made to justify the regularization claim in Section II can still be applied in the curvilinear regime. That is, even with the curvilinear transformation applied, the integrand still vanishes if h and ρ' are 0. To see this, we observe that when ρ' is small, $1 \gg \rho' \gg \rho'^2 \gg \cdots \rho'^M$. The effect of this is that as $\rho' \to 0$, the discriminant of R collapses to a linear function of ρ' and $J_c(\rho', \varphi')$ collapses to a constant, which means the integral takes the form of eqn. (2.9) and is thus subject to the same regularization argument as used in Section II when $\rho' \to 0$. Another way of thinking about this is that when $\rho' \to 0$, the scaled curvilinear polygon that maps to the scaled planar version becomes more and more planar in and of itself and in fact is exactly planar in the limit. This argument is functionally identical to the argument made in [16] to apply singularity extraction to curvilinear elements. As such, if the integrand vanishes in the planar case, it vanishes in the curvilinear case as well.

One more element of the curvilinear case that needs to be addressed is how the integrand may be computed as $f(\varphi')$ approaches 0 on the flat triangle that the curved shape is mapped to in the exact singularity case. The $f(\varphi')$ cancellations that naturally occur when $h = 0$ (see eqn. 2.9) are not as obviously obtained for higher order shapes. However, since R is a polynomial in $f(\varphi')$ as well as ρ', we may repeat the arguments above to define their behavior as $f(\varphi')$ becomes small. That is, under the above conditions, the only terms that will persist in the sum described in eqn. (5.5) are the terms that are first-order (linear) in $f(\varphi')$. All higher degree terms will be $\ll$ the first-order terms when $f(\varphi')$ is small. Under this condition, the necessary cancellations occur and the integrand may be computed without issue. Note that the only terms that persist in the J_c expression are the constant terms in the sums; J_c does not participate in these cancellations.

This now constitutes everything needed to evaluate the strongly singular integral over an arbitrary polygon. In the following sections, we will discuss some near-singularity strategies and show example computations of the eqn. (2.5) integral using the above formulation.

VI. Near-Singularity Treatment

For the above formulation, special care must be taken if the observation point is close to the source domain, but not lying exactly on it, thus creating a near-singularity. Under this circumstance, the integral computation can become unwieldy near the projected observation point, and a peak in the ρ' integrand near $\rho' = 0$ is observed, similarly to the phenomenon highlighted in [9] that motivates focused treatment of near-singular cases. During our analysis, this was empirically found to occur, with varying intensities, when the length of the vector connecting the observation point and its projection is between ~10^{-16} and 10^{-1}. Below this range, machine precision limitations impact accuracy too strongly. Above it, the spike fails to develop appreciably. To ensure accurate integration when the peak is present, we break the radial integral into several logarithmic ρ' intervals. The first interval is $[0, 10|\vec{h}|]$, the second is from $[10|\vec{h}|, 100|\vec{h}|]$, and so on until $10^N|\vec{h}|$ exceeds 0.1. Then, the rest of the integral is computed on the interval $[10^N|\vec{h}|, 1]$. This is similar in style to the "h-refinement" technique discussed in

[9], only involving far fewer sample points. The distance from $\rho' = 0$ that the spike's maximum value occurs is proportional to $|\vec{h}|$, and this interval technique was empirically found to capture the dynamics of the spike well. Smaller interval divisions are possible, but were not found to increase evaluation accuracy substantially. The ρ' integral on each interval is computed using the above formulation and Gaussian quadrature rules, as reducing the interval size creates smooth integrands in ρ'. In this way, the scaled polar formulation may be used in a general manner, even when near-singularities are involved. In the next sections, we will demonstrate the results when applying this technique to example domains.

VII. Flat Triangle Numerical Example

To demonstrate polar scaling integrand computation, we will consider the preliminary results arising from a flat triangular integration domain along with associated RWG basis functions [21]. These basis functions are defined for triangle pairs where one edge is shared between the triangles. As described in [21], for each shared edge, one triangle is the "+" triangle and one is the "–" triangle. Nominally, all of the edges of both triangles are taken to be interior to the greater domain that the triangles are partially discretizing, meaning that there are three basis functions to evaluate (see eqn. (9) of [21]). Consider a + triangle with vertices $\overrightarrow{x_1}$, $\overrightarrow{x_2}$, and $\overrightarrow{x_3}$ in Cartesian coordinates as before. Similarly to above, we may form edge vectors defined as

$$\overrightarrow{l_{21}} = \overrightarrow{x_2} - \overrightarrow{x_1}, \tag{7.1a}$$

$$\overrightarrow{l_{32}} = \overrightarrow{x_3} - \overrightarrow{x_2}, \tag{7.1b}$$

$$\overrightarrow{l_{13}} = \overrightarrow{x_1} - \overrightarrow{x_3}, \tag{7.1c}$$

and compute the triangle area as

$$A = \frac{1}{2}\left|\overrightarrow{l_{13}} \times \overrightarrow{l_{21}}\right|. \tag{7.2}$$

From here, we define the three RWG basis functions as

$$\vec{\boldsymbol{N}}_{\boldsymbol{1}}(\overrightarrow{x'}) = \frac{\left|\overrightarrow{l_{32}}\right|}{2A}\left(\overrightarrow{x'} - \overrightarrow{x_1}\right), \tag{7.3a}$$

$$\vec{\boldsymbol{N}}_{\boldsymbol{2}}(\overrightarrow{x'}) = \frac{\left|\overrightarrow{l_{13}}\right|}{2A}\left(\overrightarrow{x'} - \overrightarrow{x_2}\right), \tag{7.3b}$$

$$\vec{\boldsymbol{N}}_{\boldsymbol{3}}(\overrightarrow{x'}) = \frac{\left|\overrightarrow{l_{21}}\right|}{2A}\left(\overrightarrow{x'} - \overrightarrow{x_3}\right), \tag{7.3c}$$

where some $\overrightarrow{x'}$ lies within the triangle. Moving forward, we will focus only on $\vec{\boldsymbol{N}}_{\boldsymbol{1}}(\overrightarrow{x'})$ to represent the behavior of the presented technique, which will yield similar results to those of the other basis functions so long as the triangle's aspect ratio is sufficiently small. With this basis function, we may now evaluate eqn. (2.5). As shown in the previous sections, this integral, once transformed, consists of a double integral in ρ'-φ' space. Since the integral is singularity-free, as proved previously, it may be evaluated using one's desired choice of quadrature rules. We will choose a randomly-generated set of nodes for this exercise with vertices defined as follows:

$$\overrightarrow{x_1} = \begin{bmatrix} -0.055150912124496, \\ -0.032925442868474, \\ -0.007552809614046 \end{bmatrix}, \tag{7.4a}$$

$$\overrightarrow{x_2} = \begin{bmatrix} -0.034866643220522, \\ 0.053104972071870, \\ 0.053618399105443 \end{bmatrix}, \tag{7.4b}$$

$$\overrightarrow{x_3} = \begin{bmatrix} -0.012439806138843, \\ 0.022306317839023, \\ -0.060172988424358 \end{bmatrix}, \tag{7.4c}$$

Note that the vertices have been scaled such that the maximum triangle side-length is ~λ/5 at 500 MHz. Note that it was found that scaling the triangle between λ and λ/1000 did not affect the results given below, so the λ/5 scaling will be maintained throughout the following analysis. Here, we will largely mimic the example analysis demonstrated in [16] since that work also presents a technique to handle both near and exact singularities with the same method, as noted in Section I of this paper (though, again, the method presented in [16] requires non-general analytical treatment). In [16], 4 cases for planar triangles are discussed; one with the observation point placed on the triangle centroid, one with the point offset from the centroid by a distance of λ/100 in the direction normal to the triangle plane, one with the point placed on a triangle edge (we select the midpoint of e_{32} edge here), and one offset from the edge point by λ/100 in a plane-normal direction. Note that the triangle in [16] was also scaled to λ/5, though its exact vertex definition is not listed. Following the polar scaling procedures described above, we may evaluate eqn. (2.5). Here, for demonstrative purposes, we will compute the φ' integral first and plot the resulting ρ' integrand as a function of ρ' to show that it is finite and continuous when $\rho' = 0$. That is, we may represent the integral we wish to evaluate as

$$\int_0^1 \int_0^{2\pi} I'(\rho', \varphi') d\varphi' d\rho', \tag{7.5}$$

and we will plot the function

$$g(\rho') = \int_0^{2\pi} I'(\rho', \varphi') d\varphi' \tag{7.6}$$

to show integrand existence and continuity for all ρ' values. Note that $I'(\rho', \varphi')$ may be found by following procedures similar to those outlined in eqns. (2.5)-(2.9), only for all the terms in the eqn. (2.5) brackets. Doing this, we obtain the integrand functions shown in Fig. 4 for the $\vec{\boldsymbol{N}}_{\boldsymbol{1}}(\overrightarrow{x'})$ basis functions when the observation point is placed at the centroid with and without the offset, respectively. Fig. 4 also shows the

real part of the integrand when the offset is λ/10000 in order to better demonstrate the peak property discussed in the previous section (note the imaginary part does not display a similar peak). As shown by these plots, the ρ' integrands for an observation point lying on the source domain are indeed smooth and continuous for all values of ρ' including $\rho' = 0$, where the integrand vanishes. For all of these integrand plots, the $g(\rho')$ values were computed using Gaussian quadrature rules with 101 sample points per active edge (303 points in total for the full angular integral; note that this number of points will change during convergence studies, as will be detailed below). In addition, we will plot $f(\varphi')$ (see eqn. (4.8)) as well as the following expression:

$$g(\varphi') = I'(1, \varphi')\,. \tag{7.7}$$

Note that ρ' is set to 1 in eqn. (7.7), but the choice of ρ' does not affect the macroscopic behavior of the expression in terms of smoothness. The plots for these two functions confirm the claim that the angular portions of the transformed integrals do not behave in a manner that would introduce numerical issues. Note that the triangle vertices are located approximately at $\varphi' = -44°$, 88°, and 214°. As Fig. 5 illustrates, the angular functions exhibit piecewise behavior in the intervals between these points. The piecewise functions share the same values at the intersections between the intervals, though the derivatives are not necessarily continuous at these points. This is not an issue, though, as each interval receives its own integral in the full evaluation, so derivative continuity is not required at the vertices. Within the intervals, Fig. 5 shows sufficient smoothness for efficient numerical integration.

To examine the convergence dynamics, we plot the asymptotic behavior of the integral evaluations as the number of Gaussian quadrature sample points is increased. This will be done for the 4 cases described above. For simplicity, we will keep the number of sample points the same for both the angular and radial integrals, though this is not required. Figs. 6-7 demonstrate the convergence for the integral evaluation. The plots show the number of correct significant digits past the decimal point compared to a reference value obtained from using 101 sample points per integral. That is, we plot the value D defined as

$$D(N) = avg\left(-log\left(\frac{|I_N - I_{101}|}{|I_{101}|} + 1 \times 10^{-16}\right)\right), \tag{7.8}$$

where I_N is a component (x, y, or z) of the of the integral evaluation using N sample points, I_{101} is the evaluation of that component for 101 sample points, and 1×10^{-16} is added to ensure the number of digits does not exceed machine precision. The number of digits for each component is then

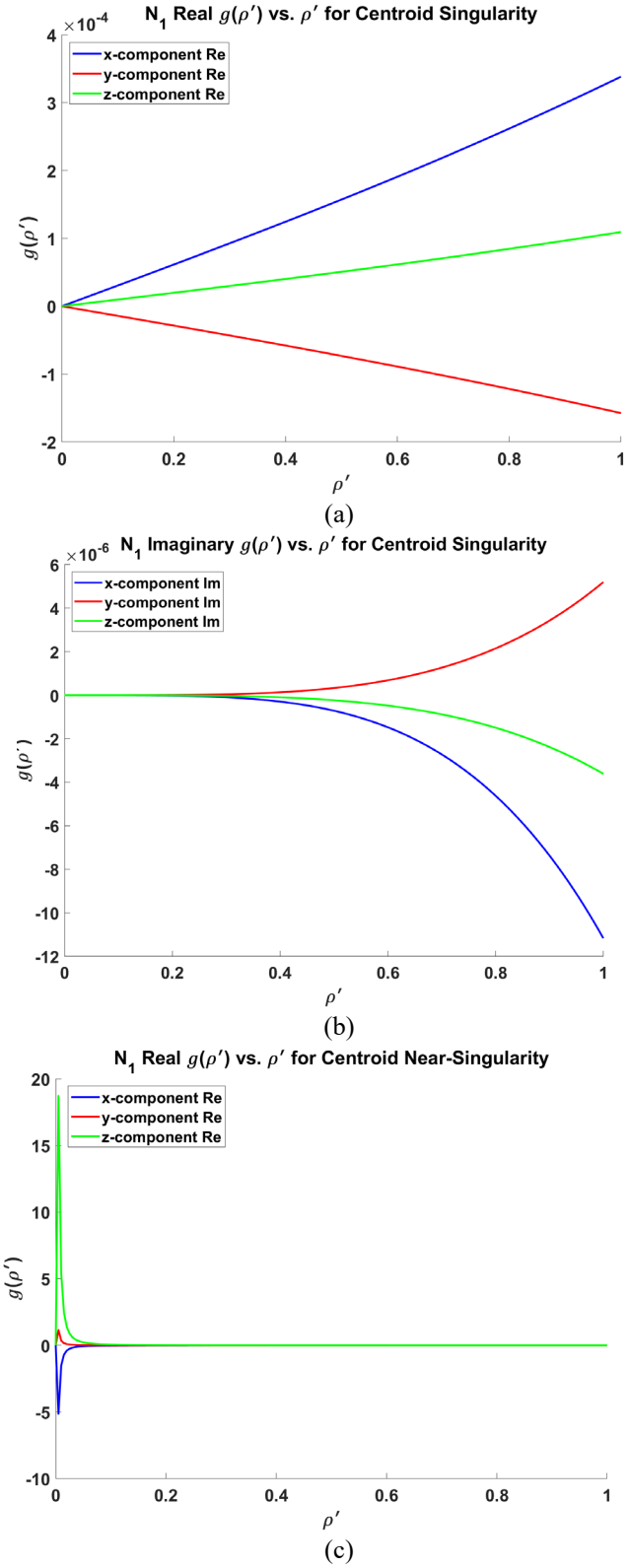

Fig. 4. $\vec{N}_1(\vec{x'})$ ρ' integrand real part (a) and imaginary part (b) for centroid exact singularity. (c) shows the real part delta-function-like behavior of the real part of the integrand for the case of a λ/10000 near-singularity.

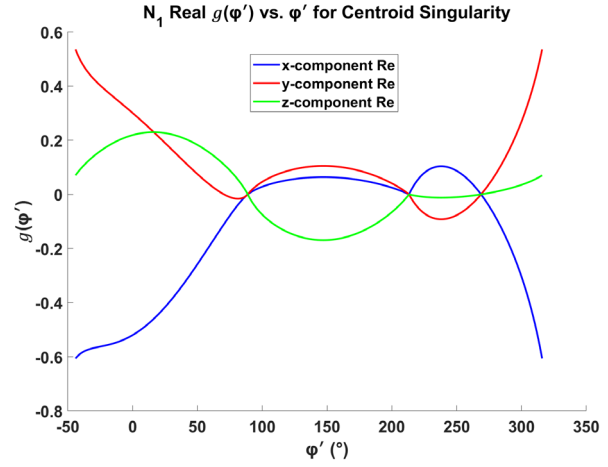

(a)

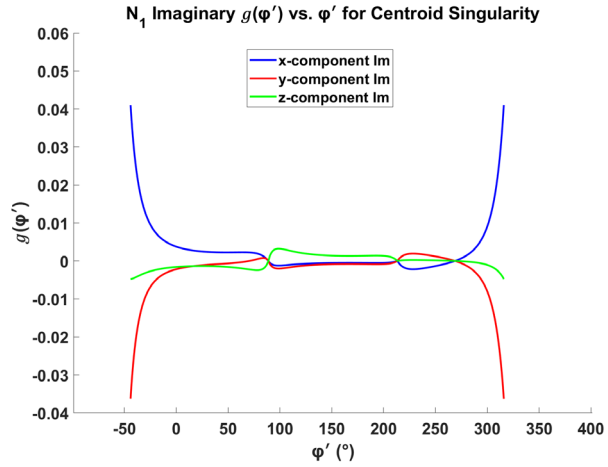

(b)

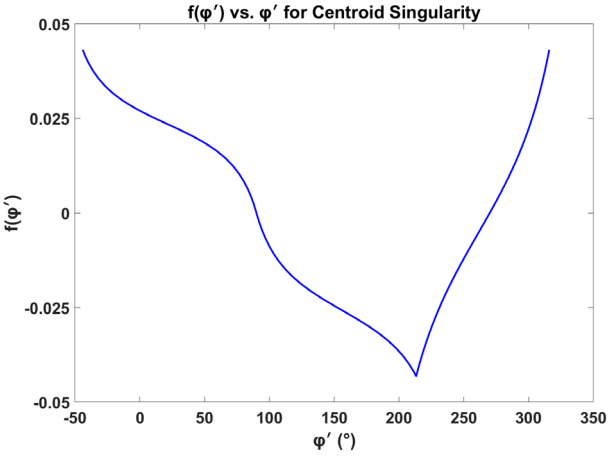

(c)

Fig. 5. $\vec{N}_1(\vec{x'})$ integrand $g(\varphi')$ real part (a) and imaginary part (b), as well as $f(\varphi')$ for the triangle under study (c).

averaged across all vector components and all three basis functions to represent the overall number of correct digits. The convergence curves are then compared to results obtained in [16] for a similar triangle. The two additional curves shown on each plot are the results for the integral evaluated using the method proposed in [16], termed "RA-1", and conventional singularity extraction (subtraction), termed "SS". Note that, as alluded to in the introduction of this paper, the "RA-1" method

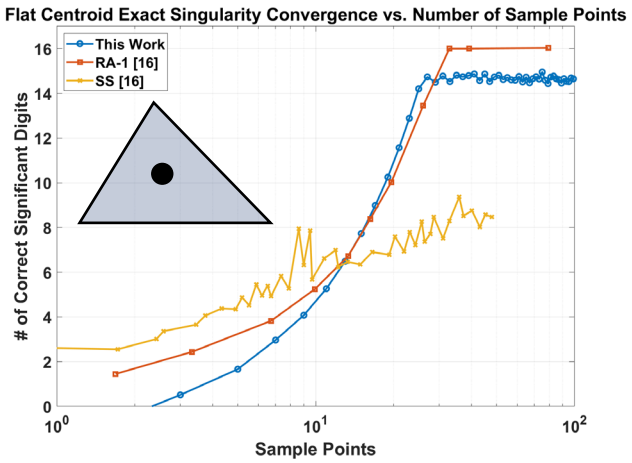

(a)

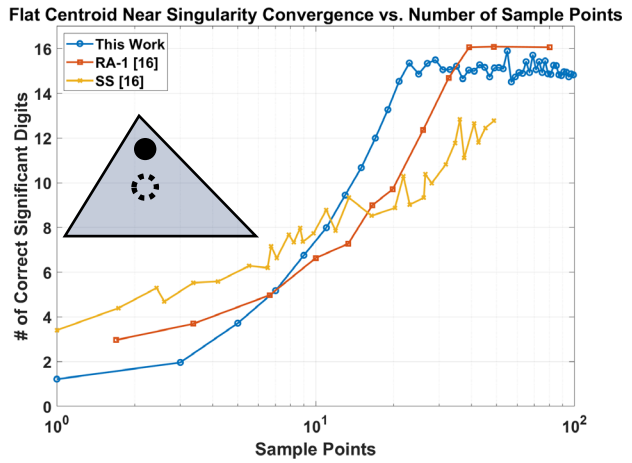

(b)

Fig. 6. Convergence results vs. base sample points for a flat triangle with centroid evaluation point exact singularity (a) near-singularity (b).

of [16] combines singularity extraction with a singularity cancellation technique to create a method that can handle both exact and near singularities. In this sense, the RA-1 method is not fully numerical like the technique presented in this work. Nevertheless, the RA-1 is indeed quite powerful and state-of-the-art, so comparison between it and the proposed method is demonstrative. Note that [16] also contains near-singularity convergence results for integrals evaluated using singularity cancellation ("SC") alone. However, since those curves do not outperform the RA-1 curves and do not apply to exact singularities, the SC results are not shown here. Note also that in [16], the convergence results are split between the normal and tangential components of the integral result. For each case presented here, the component that displayed superior (faster) convergence was selected for comparison so as not to shortchange the results of the previous works. Fig. 8 also shows the convergence results of this work only all on the same plot for comparison.

The actual 101 point evaluated reference values of these test integrals are listed in Table I for the $\vec{N}_1(\vec{x'})$ basis function. Note the total number of Gaussian quadrature evaluations for both the angular and radial integrals is $3N^2$ for the exact singularities (N points for the angular integral and N points for

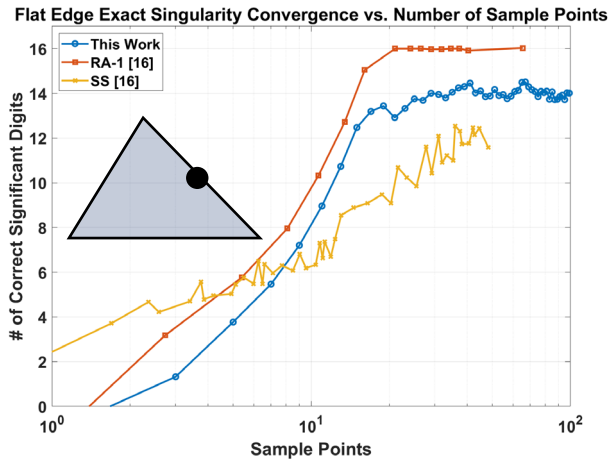

(a)

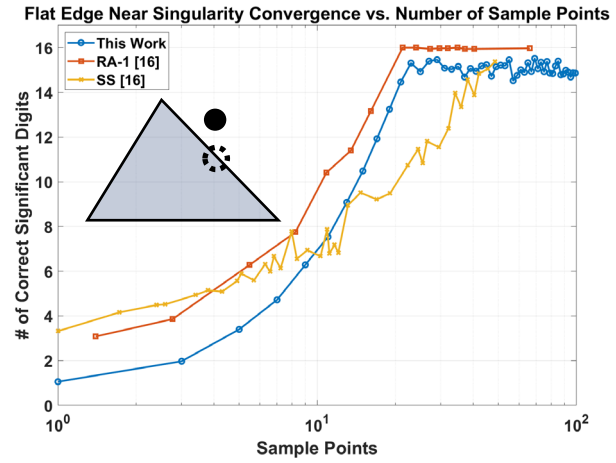

(b)

Fig. 7. Convergence results for flat triangle with edge midpoint evaluation point exact singularity (a) near-singularity (b).

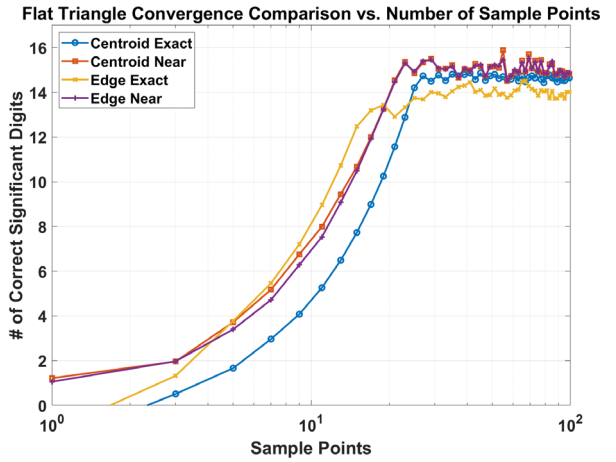

Fig. 8. Comparison of flat triangle convergence for all investigated cases evaluated using the polar scaling technique.

the radial integral per edge) and $9N^2$ for the near-singularities since 3 intervals are used for the near-singularity. We will refer to the value N as the number of "base" sample points going forward. For the centroid singularities, the precision of the proposed method saturates by ~20-30 base sample points with saturation values very close to machine precision. The centroid singularity convergence rate of the proposed technique indeed compares quite favorably to that exhibited by the RA-1 method and outperforms the SS results for moderate to high precision. For the edge singularities, saturation occurs by ~20-30 base sample points as well, with a somewhat slower convergence rate than the RA-1 counterpart while still showing superior convergence to the SS method beginning at ~10 sample points. Even so, the convergence rate of the proposed technique is not slower than RA-1 by a major amount and is still competitive. Note that the saturation precision of the proposed method appears to be 14-15 digits for all cases as opposed to the 16 digit machine precision, but this is not taken as a strong detriment for any practical application, as the difference of 1 or 2 digits will certainly be overwhelmed by error introduced by other factors of a full-wave simulation such as the geometric fidelity of the model.

To continue our analysis, we will examine the convergence effects of deforming the triangle to reduce its quality. To quantify the quality of the triangle, we will use the following Figure of Merit (FoM) similar to that proposed in [22]:

$$FoM = 4\sqrt{3}\frac{A}{\sqrt{\left|\overrightarrow{l_{21}}\right|^2 + \left|\overrightarrow{l_{32}}\right|^2 + \left|\overrightarrow{l_{13}}\right|^2}}, \tag{7.9}$$

where the variables are defined as in eqn. (7.1) and eqn. (7.2). To deform the triangle, we will take $\overrightarrow{x_1}$ and move it toward the edge connecting $\overrightarrow{x_2}$ and $\overrightarrow{x_3}$ (e_{32}) along the line connecting $\overrightarrow{x_1}$ and its projection onto edge e_{32}, making the triangle thinner and thinner. We will then represent the convergence rate by tracking the amount of correct digits obtained for 10 base sample point integral evaluations. Fig. 9 shows this result. Note that the highest FoM shown corresponds to the nominal triangle with no movement of $\overrightarrow{x_1}$. As the figure demonstrates, the convergence rate does indeed degrade as the triangle quality is reduced, taking a somewhat linear degradation. This result is not unexpected, as lower-quality triangles typically lead to a marked reduction in numerical tractability for such problems as those investigation here. Still, the convergence variation shown in Fig. 9 does not indicate any major weaknesses of the formulation presented in this work.

Finally, we will investigate the convergence dynamics of changing a near-singularity's position relative to the triangle interior. To do this, we will place the near-singularity at a distance of λ/100 away from the midpoint of e_{32} and rotate its position about the e_{32} axis. Fig. 10 shows this process. For edge rotation angles between 0° and 90°, the near-singularity is positioned above the triangle interior, making its projection within interior to the triangle as well. Meanwhile, when the angle is between 90° and 180°, the projection lies exclusively on the triangle edge. The effect of the positioning on the convergence rate is again evaluated by looking at the number of correct digits using 10 base sample points. Fig. 11 indicates that the convergence rate increases markedly once the projection of the evaluation point is on the edge of the triangle, though there is no angle for which the convergence rate is compromised to the point of un-usability.

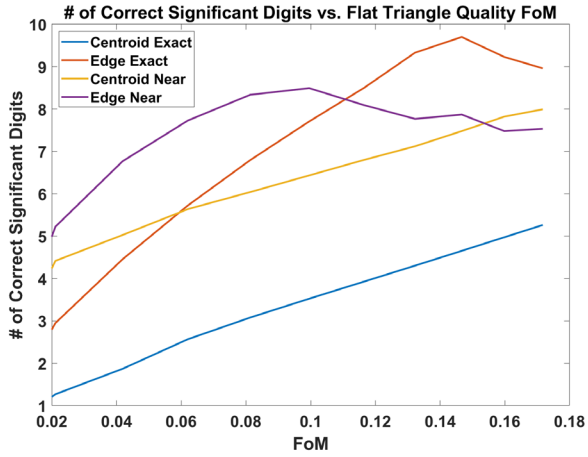

Fig. 9. 10 sample point convergence as a function of triangle FoM.

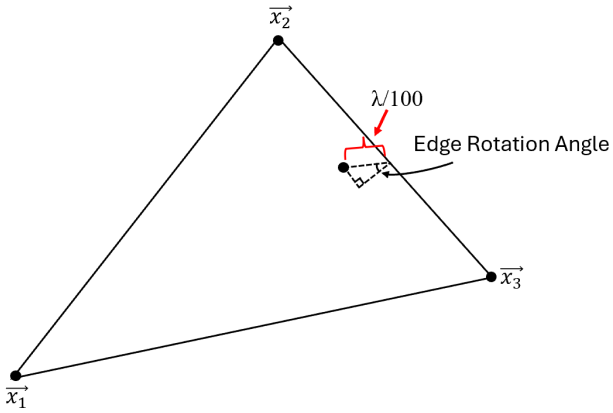

Fig. 10. Rotation of near-singularity about the e_{32} axis.

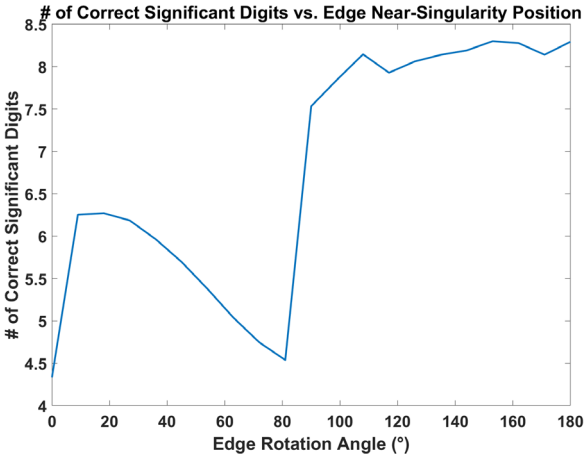

Fig. 11. Convergence rate of the near-singularity as a function of the rotation angle about the e_{32} axis.

This is interesting, as it shows that the proposed technique prefers the projection of the evaluation point to lie outside the triangle interior, at least when the evaluation point is near the edge. The exact reason for this is not clear, but warrants further investigation in the future.

This concludes the analysis for the case of a flat triangle. In the next section, the analysis will be repeated for a quadratic curvilinear version of similar scale.

VIII. Curvilinear Triangle Numerical Example

To define our curvilinear triangle to investigate, we start with the vertices defined in eqn. (7.4). We will call these vertices the "base nodes". We then define 3 additional nodes by starting at the midpoints of the straight edges connecting the vertices and then moving those points a distance of λ/50 in the direction normal to the plane of the triangle defined in the previous section, creating curvature. We define this λ/50 value as the "curvature height" (we will use this definition later for triangle deformation tests). Using these 6 points, we apply the mapping procedure discussed in Section V to define a projected flat triangle in (u', v') space and conduct the polar scaling integration. For our basis functions, we use RWG-like basis functions created using the (u', v') mapping formalism developed here. These basis functions retain the rooftop quality of the conventional RWG basis functions as well as the divergence-conforming characteristic. The detailed explanation of the basis function development is presented in Appendix A. Note that for this analysis, the functions were scaled based on Euclidean distance rather than arc length (see Appendix A). Here, we run the same convergence experiments as were presented in the previous section, again comparing the results to those shown in [16]. The $\vec{\boldsymbol{C}}_{\boldsymbol{1}}(\overrightarrow{r'})$ basis function evaluations for these experiments are given in Table II. It should be noted that the exact node positions for the triangles analyzed in [16] are not given and that different edges appear to be used for the near and exact singularity results (see Figs. 12 and 13 of [16]), but it is assumed based on the results that the dimensions and curvature are comparable. In Figs. 12-14, the convergence results are given for the same evaluation point placements as in the previous section. Examining these results, we see that the proposed technique vastly outperforms the SS method and moderate and high precision for all cases. It is also seen that, interestingly, the proposed technique shows consistently better convergence than the RA-1 method at moderate precision, but then is passed as both methods approach saturation. A possible reason for this could be due to the presented curvilinear formulation. As detailed in Section V, a mapping is conducted by solving a matrix equation based on the number of given nodes to find polynomial mapping coefficients. These coefficients, by necessity, only approximate the mapping for the entire shape, with more coefficients providing a more accurate mapping. As more points are used in the integral evaluation, any error introduced by the finite resolution of the mapping can impact, but not destroy, the precision values when such values become extreme. On the other hand, the curvilinear formulation used in [16] appears to rely on area coordinates defined using Lagrange Interpolation Functions [23], which increase the complexity of the mapping but offer higher-quality interpolation. This could be the source of the convergence differences. Perhaps the polar scaling curvilinear extension can be revisited using Lagrange Interpolation Functions, but this will be reserved for future work. In any case, the convergence rate of the proposed technique is fast enough to justify its consideration in comparison to the RA-1 technique, recalling that the latter method is not general since it requires analytical treatment. Next, we will deform the triangle formed from the base nodes (which also forms the flat projected triangle in our curvilinear formulation; see Fig. 3) in the exact same manner

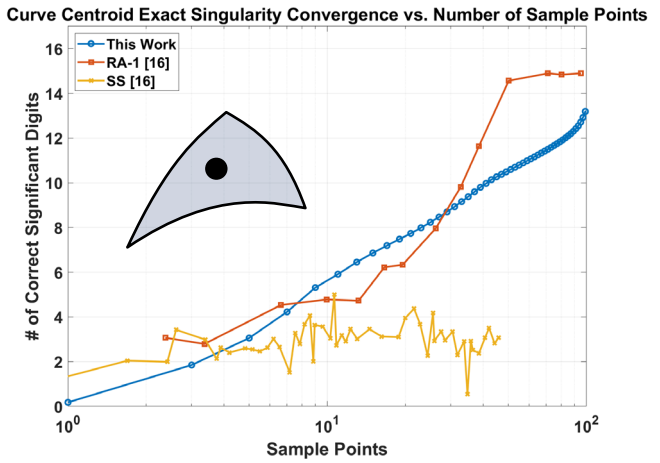

(a)

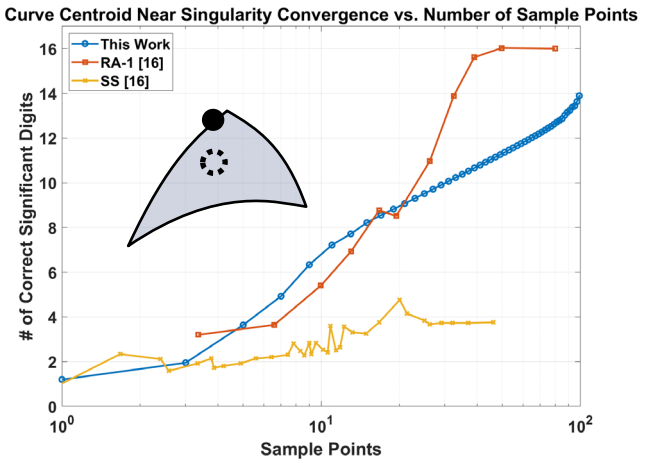

(b)

Fig. 12. Convergence results vs. base sample points for a curvilinear triangle with centroid evaluation point exact singularity (a) near-singularity (b).

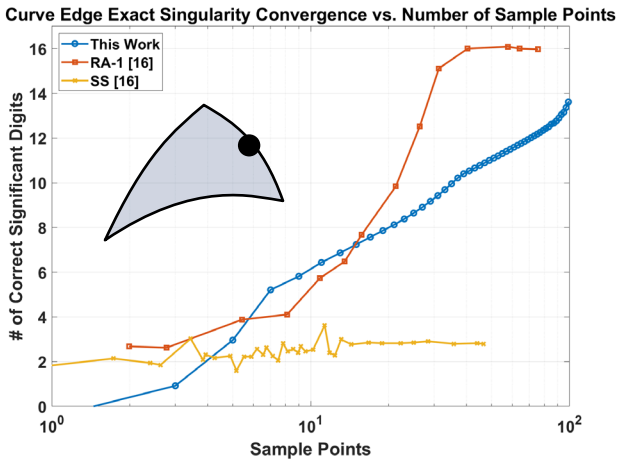

(a)

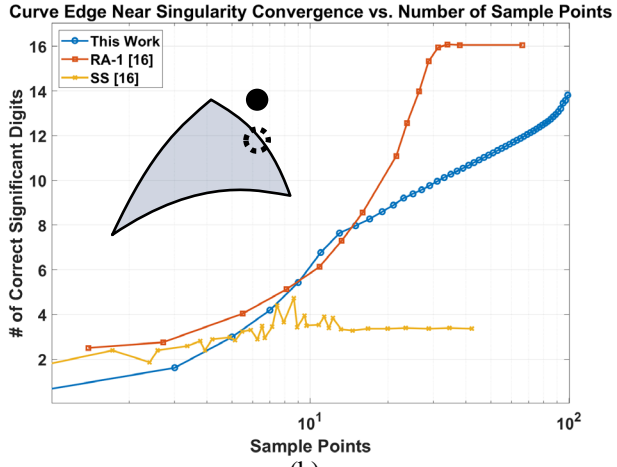

(b)

Fig. 13. Convergence results vs. base sample points for a curvilinear triangle with edge evaluation point exact singularity (a) near-singularity (b).

as the triangle in the previous section and investigate the convergence effects as a function of the projected triangle FoM defined by eqn. (7.9). The results of this are shown in Fig. 15. As before, reducing the quality of the base triangle negatively impacts the convergence rate of the integration, but again, the formulation appears to be robust enough to not be debilitated rapidly when the triangle quality reduces.

Finally, we will examine the convergence effects of increasing the triangle curvature while keeping the base triangle constant at is nominal shape. To do this, we will sweep the curvature height between λ/50 and λ/5. The results of this study are given in Fig. 16. As expected, increasing the curvature decreases the convergence rate, which is likely due to the weakening of the mapping approximation as the curvature becomes more extreme. Nevertheless, again, high deformation does not render the proposed technique un-usable, as the convergence, while degraded, is not invalidated.

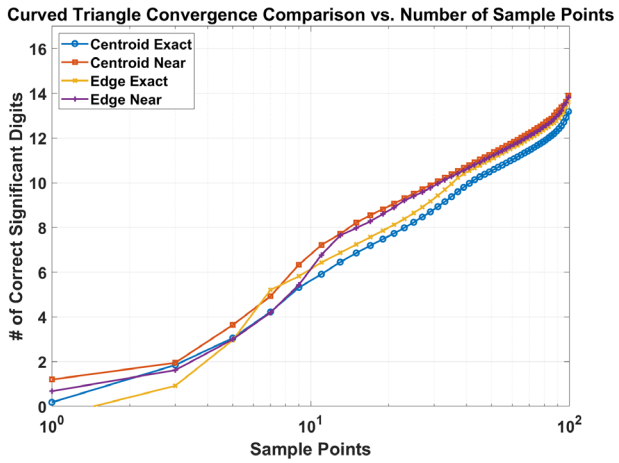

Fig. 14. Comparison of curved triangle convergence for all investigated cases evaluated using the polar scaling technique.

IX. Conclusion

In this work, we have demonstrated a powerful polar transformation technique that eliminates the strong singularity found in common Helmholtz surface integrals used in MoM formulations regardless of observation point position. The technique is applicable to any non-singular basis function and straight-edged planar or curvilinear shape, making it highly versatile compared to singularity extraction techniques, which require a new analytical integral to be evaluated for each type of shape and basis function. Moreover, the polar scaling formalism is intrinsically open to extension to higher order surfaces and more sophisticated edge geometries. Furthermore,

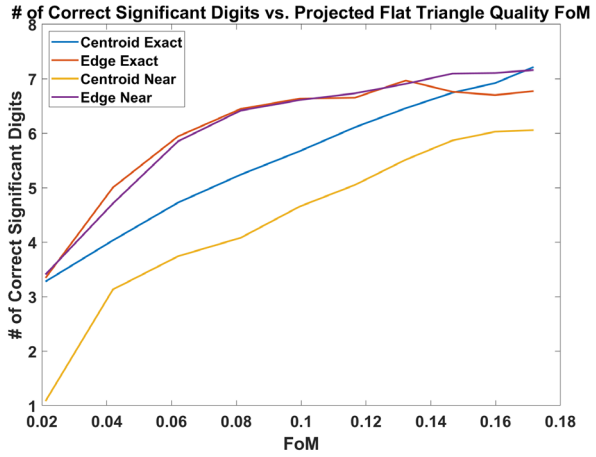

Fig. 15. 10 sample point convergence as a function of projected triangle FoM.

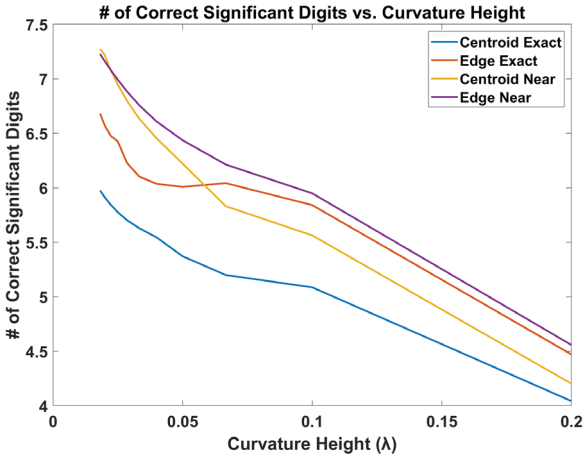

Fig. 16. 10 sample point convergence as a function of curvature height.

this work mathematically proves that the Helmholtz strongly singular integral is convergent and specifies the explicit principal value of the integrand at the singularity, whereas no such evaluation has been made readily available in the literature for this case before now. The technique of this work also has been shown to achieve precision on par with similar methods while offering greater generality. As such, the technique proposed here represents a powerful method for evaluating Helmholtz integrals over 2D straight/curved domains.

APPENDIX A: CURVILINEAR TRIANGLE RWG BASIS FUNCTIONS

For this work, RWG-like basis functions were developed for curvilinear triangular shapes of arbitrary order. These basis functions were designed with the following properties in mind:

1. Like the conventional planar RWG basis function, each curvilinear function must have a "rooftop-like" profile with respect to a shared edge between two curvilinear triangles, with the functions reaching their maximum values at the shared edge.
2. The functions must be tangential to the curvilinear shape's surface at all points in the shape domain.

TABLE I
$\vec{N}_1(\vec{r'})$ FLAT TRIANGLE INTEGRAL RESULTS

Position	Exact Singularity	Near − Singularity
Centroid	$(0.000161203717652 - 0.000002251673733j)\hat{x}$ $+ (-0.000075040899677 + 0.000001048162072j)\hat{y}$ $+ (0.000052081694088 - 0.000000727470707j)\hat{z}$	$(-0.074835904131704 + 0.000153651741319j)\hat{x}$ $+ (0.017387341770886 - 0.000036335312426j)\hat{y}$ $+ (0.274792700073766 - 0.000537141740016j)\hat{z}$
Edge	$(-0.0006852559009511 + 0.000005088303876j)\hat{x}$ $+ (0.000318989041105 - 0.000002368623418j)\hat{y}$ $+ (-0.000221392463681 + 0.000001643929121j)\hat{z}$	$(-0.103568200417083 + 0.000160767847553j)\hat{x}$ $+ (0.030794257217944 - 0.000038938318873j)\hat{y}$ $+ (0.182176162745084 - 0.000532913386629j)\hat{z}$

TABLE II
$\vec{C}_1(\vec{r'})$ CURVILINEAR TRIANGLE INTEGRAL RESULTS

Position	Exact Singularity	Near − Singularity
Centroid	$(-0.004444190995035 + 0.000004051669403j)\hat{x}$ $+ (-0.011236180468949 + 0.000000349778635j)\hat{y}$ $+ (-0.009476922031595 - 0.000002531356276j)\hat{z}$	$(-0.074518090511891 + 0.000164855959553j)\hat{x}$ $+ (0.010192675190397 - 0.000037584862160j)\hat{y}$ $+ (0.256426576930666 - 0.000554916795460j)\hat{z}$
Edge	$(-0.008717979624414 + 0.000013887597464j)\hat{x}$ $+ (-0.004123591155202 - 0.000006713955664j)\hat{y}$ $+ (-0.003971112418414 - 0.000002366391620j)\hat{z}$	$(-0.116416533969791 + 0.000174539936228j)\hat{x}$ $+ (0.045983443106824 - 0.000043818344172j)\hat{y}$ $+ (0.212494211465247 - 0.000553096661029j)\hat{z}$

3. At the shared edge between the curvilinear shapes, the basis function component normal to the shared edge contour must be continuous between the + and – triangles.

To create functions with these properties, we will make use of the (u', v') mapping outlined in Section V. Consider a + curvilinear triangle with three basis functions $\vec{C}_1(\vec{r'})$, $\vec{C}_2(\vec{r'})$, and $\vec{C}_3(\vec{r'})$, each corresponding to a vertex and shared edge with a – triangle. We will consider only $\vec{C}_1(\vec{r'})$ moving forward, as the analysis is identical for the other two functions. This function will correspond to vertex 1 of the shape. The curvilinear triangle may be mapped to a planar version in (u', v') space as per the procedure in Section V. Using this mapping, we may define a unique contour on the curvilinear shape that extends from the vertex of choice to the point where the basis function is being evaluated. This contour will be defined as the curvilinear contour that contains every point on the straight line from the vertex to the evaluation point in (u', v') space, as illustrated in Fig. A1. We will label this contour $\vec{l_a}$, where $|\vec{l_a}|$ is the arc length of the contour and the

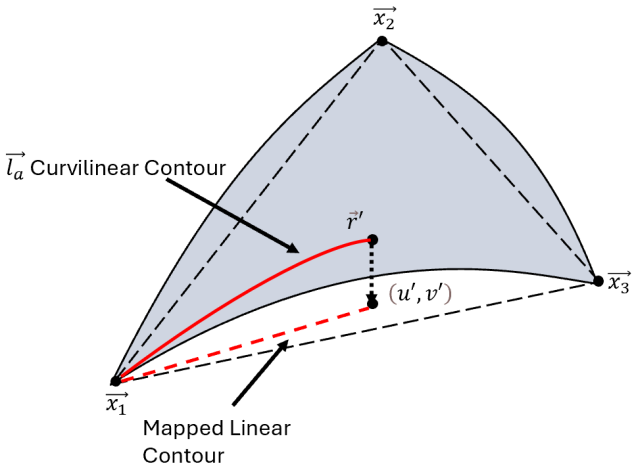

Fig. A1. $\vec{l}_a$ contour on the curvilinear shape and mapped linear contour on projected shape.

direction of $\vec{l}_a$ is the direction the contour is pointing in at the basis function evaluation point. Let (u_0', v_0') be the basis function evaluation point in (u', v') space. Then the line connecting the vertex 1 point (u_1, v_1) and the evaluation point in (u', v') space is:

$$v' = m_0(u' - u_1) + v_1, \tag{A.1a}$$

with

$$m_0 = \frac{(v_0' - v_1)}{(u_0' - u_1)}. \tag{A.1b}$$

At every point $\vec{r}'$ on the curvilinear contour defined by this line, we observe, using the notation defined in Section V,

$$d\vec{r}' = \frac{\partial \vec{r}}{\partial u'}du' + \frac{\partial \vec{r}}{\partial v'}dv' = \left(\frac{\partial \vec{r}}{\partial u'} + \frac{\partial \vec{r}}{\partial v'}\frac{dv'}{du'}\right)du'. \tag{A.2a}$$

As such, the arc length $|\vec{l}_a|$ may be computed as

$$|\vec{l}_a| = \int_{u_1}^{u_0'} \left|\left(\frac{\partial \vec{r}}{\partial u'} + \frac{\partial \vec{r}}{\partial v'}\frac{dv'}{du'}\right)\right| du'$$

$$= \int_{u_1}^{u_0'} \left| \begin{array}{l} \sum_{i=0}^{M}\sum_{j=0}^{i}(i-j)\vec{b}_{ij}(u'-u_0)^{i-j-1}[m_0(u'-u_1)+v_1-v_0]^j \\ +m_0\sum_{i=0}^{M}\sum_{j=0}^{i}(j)\vec{b}_{ij}(u'-u_0)^{i-j}[m_0(u'-u_1)+v_1-v_0]^{j-1} \end{array} \right| du' \tag{A.3}$$

Where eqn. (5.1) has been substituted in ad differentiated. This integral may be easily integrated numerically. Meanwhile, the direction of $\vec{l}_a$ is the unit vector pointing in the direction of $\frac{d\vec{r}}{du'}$ at the evaluation point, which, after some algebraic manipulations, leads to

$$\hat{l}_a = \frac{\vec{D}}{|\vec{D}|}, \tag{A.4a}$$

$$\vec{D} = \sum_{i=0}^{M}\sum_{j=0}^{i} \vec{b}_{ij}(u_0' - u_0)^{i-j-1}[m_0(u_0' - u_1) + v_1 - v_0]^{j-1} * [(i-j)(m_0(u_0' - u_1) + v_1 - v_0) + m_0 j(u_0' - u_0)]. \tag{A.4b}$$

If we use $\vec{l}_a$ to scale our basis function, properties 1 and 2 above will be satisfied, given that the magnitude of this vector increases from 0 as the contour running from the vertex to the shared edge is approached and its direction is tangential to the curvilinear shape by definition. To satisfy the third property, we must find the component of $\vec{l}_a$ that is normal to the shared edge contour at all points on the edge and normalize the basis function by this value. Since the shared edge is defined by the line connecting (u_2, v_2) and (u_3, v_3) in (u', v') space, we may define the shared edge contour according to the line

$$v_e' = m_e(u_e' - u_2) + v_2, \tag{A.5a}$$

with

$$m_e = \frac{(v_3 - v_2)}{(u_3 - u_2)}. \tag{A.5b}$$

Using the same analysis as above, we may represent the vector parallel to the edge contour at any point on the edge as

$$\hat{e} = \frac{\vec{E}}{|\vec{E}|}, \tag{A.6a}$$

$$\vec{E} = \sum_{i=0}^{M}\sum_{j=0}^{i} \vec{b}_{ij}(u_e' - u_0)^{i-j-1}[m_e(u_e' - u_2) + v_2 - v_0]^{j-1} * [(i-j)(m_e(u_e' - u_2) + v_2 - v_0) + m_e j(u_e' - u_0)]. \tag{A.6b}$$

For any contour represented by $\vec{l}_a$ that intersects with the shared edge, the dot product of $\hat{l}_a$ and the local in-plane edge normal vector is equal to the cosine of the angle between $\hat{l}_a$ and the edge normal vector, which is equal to the sine of the angle between $\hat{l}_a$ and the edge tangent vector $\hat{e}$. Therefore, at the edge point, the edge normal component of $\vec{l}_a$ is

$$\vec{l}_{a\perp} = |\vec{l}_a||\hat{l}_a \times \hat{e}|. \tag{A.7}$$

For each (u_0', v_0'), there is only one line that connects vertex 1 and the evaluation point that intersects with the shared edge. To find the point (u_{ae}', v_{ae}') where this occurs, we merely develop the following system of equations from the expressions for the evaluation and edge lines in (u', v') space:

$$\begin{bmatrix} -m_0 & 1 \\ -m_e & 1 \end{bmatrix}\begin{bmatrix} u_{ae}' \\ v_{ae}' \end{bmatrix} = \begin{bmatrix} v_1 - m_0 u_1 \\ v_2 - m_e u_2 \end{bmatrix}, \tag{A.8}$$

which has the solution

$$\begin{bmatrix} u_{ae}' \\ v_{ae}' \end{bmatrix} = \frac{1}{m_e - m_0}\begin{bmatrix} v_1 - v_2 - m_0 u_1 + m_e u_2 \\ m_e v_1 - m_0 v_2 + m_0 m_e (u_2 - u_1) \end{bmatrix}. \tag{A.9}$$

With this, we finally arrive at the curvilinear RWG basis function:

$$\vec{\boldsymbol{C}}_{\mathbf{1}}(\overrightarrow{r'}) = \frac{\overrightarrow{l_a}}{\left|\overrightarrow{l_{ae}}\right|\left|\widehat{l_{ae}} \times \widehat{e_{ae}}\right|}, \qquad (A.10)$$

where the quantities in the denominator are the values of eqn. (A.3), eqn. (A.4), and eqn. (A.6) evaluated at the point (u_{ae}', v_{ae}') solved in eqn. (A.9) and $\overrightarrow{l_a}$ is evaluated as per the procedure outlined above for an evaluation point (u_0', v_0') in (u', v') space. The normalization in the denominator guarantees that the normal component will always have a magnitude of 1 at the shared edge, asserting the property 3 continuity. $\vec{\boldsymbol{C}}_{\mathbf{2}}(\overrightarrow{r'})$ and $\vec{\boldsymbol{C}}_{\mathbf{3}}(\overrightarrow{r'})$ may be formed using identical methods for the other two sets of vertices and shared edges. The basis function for a – triangle is merely eqn. (A.10) with a negative sign and quantities defined by the – triangle vertex in (u', v') space opposite the shared edge.

Alternatively, $\vec{\boldsymbol{C}}_{\boldsymbol{n}}(\overrightarrow{r'})$ may be scaled according to the Euclidean distance from the evaluation point to the relevant vertex on the mapped planar triangle. That is, for the basis function extending from vertex 1, $\left|\overrightarrow{l_a}\right|$ would be equal to the length of the vector connecting (u_1, v_1) and (u_0', v_0') in (u', v') space. Formulating the basis functions this way eliminates the need to compute an arc length integral for each evaluation while maintaining the rooftop-like quality and normal component continuity on shared edges. The drawback is that the basis function no longer increases in magnitude uniformly along the contour connecting the vertex to the evaluation point on the curvilinear shape. However, for triangles of sufficiently-low curvature, the effect of this should not be stark. Full understanding of such curvature limitations would require comparisons of full-wave integration results using both function types and is beyond the scope of this work.

REFERENCES

[1] R. D. Graglia, "On the numerical integration of the linear shape functions times the 3-D Green's function or its gradient on a plane triangle," in *IEEE Transactions on Antennas and Propagation*, vol. 41, no. 10, pp. 1448-1455, Oct. 1993, doi: 10.1109/8.247787.

[2] Ilari Hanninen, Matti Taskinen, and Jukka Sarvas, "Singularity Subtraction Integral Formulae for Surface Integral Equations with RWG, Rooftop and Hybrid Basis Functions," in *Progress In Electromagnetics Research*, Vol. 63, 243-278, 2007. doi:10.2528/PIER06051901.

[3] M. S. Tong and W. C. Chew, "A Novel Approach for Evaluating Hypersingular and Strongly Singular Surface Integrals in Electromagnetics," in *IEEE Transactions on Antennas and Propagation*, vol. 58, no. 11, pp. 3593-3601, Nov. 2010, doi: 10.1109/TAP.2010.2071370.

[4] M. S. Tong and W. C. Chew, "Super-hyper singularity treatment for solving 3D electric field integral equations," *Microw. Opt. Technol. Lett.*, vol. 49, pp. 1383–1388, 2007.

[5] A. Herschlei, J. V. Hagen, and W. Wiesbeck, "Methods for the Evaluation of Regular, Weakly Singular and Strongly Singular Surface Reaction Integrals Arising in Method of Moments", *ACES Journal*, vol. 17, no. 1, pp. 63–73, Jul. 2022.

[6] R. D. Graglia and G. Lombardi, "Machine precision evaluation of singular and nearly singular potential integrals by use of Gauss quadrature formulas for rational functions," in *IEEE Trans. Antennas Propag.*, vol.56, pp. 981–998, 2008.

[7] P.W. Fink, D. R.Wilton, and M. A. Khayat, "Issues and methods concerning the evaluation of hypersingular and near-hypersingular integrals in BEM formulations," presented at the Int. Conf. Electromagnetics in Advanced Applications, Torino, Italy, Sep. 2007.

[8] F. Vipiana and D. R. Wilton, "Numerical Evaluation via Singularity Cancellation Schemes of Near-Singular Integrals Involving the Gradient of Helmholtz-Type Potentials," in *IEEE Transactions on Antennas and Propagation*, vol. 61, no. 3, pp. 1255-1265, March 2013, doi: 10.1109/TAP.2012.2227922.

[9] P. W. Fink, D. R. Wilton and M. A. Khayat, "Simple and Efficient Numerical Evaluation of Near-Hypersingular Integrals," in *IEEE Antennas and Wireless Propagation Letters*, vol. 7, pp. 469-472, 2008, doi: 10.1109/LAWP.2008.2000788.

[10] M. D. Zhu, T. K. Sarkar, Y. Zhang and M. Salazar-Palma, "A Novel Framework of Singularity Cancellation Transformations for Strongly Near-Singular Integrals," in *IEEE Transactions on Antennas and Propagation*, vol. 69, no. 12, pp. 8539-8550, Dec. 2021, doi: 10.1109/TAP.2021.3083834.

[11] Ismatullah and T. F. Eibert, "Adaptive Singularity Cancellation for Efficient Treatment of Near-Singular and Near-Hypersingular Integrals in Surface Integral Equation Formulations," in *IEEE Transactions on Antennas and Propagation*, vol. 56, no. 1, pp. 274-278, Jan. 2008, doi: 10.1109/TAP.2007.913170.

[12] M. G. Duffy, "Quadrature over a pyramid or cube of integrands with a singularity at a vertex," *SIAM J. Numer. Anal.*, vol. 19, no. 6, pp.1260–1262, 1982.

[13] P. W. Fink and M. A. Khayat, "A simple transformation for the numerical evaluation of near strongly singular integrals," IEEE Antennas and Wireless Propagation Letters, 12: 225–228, 2013.

[14] M. Guiggiani, "The Evaluation of Cauchy Principal Value Integrals in the Boundary Element Method—a Review," in *Mathematical and Computer Modelling*, Volume 15, Issues 3–5, 1991, Pages 175-184.

[15] M. Guiggiani, A. Gigante, "A General Algorithm for Multidimensional Cauchy Principal Value Integrals in the Boundary Element Method," in *J. Appl. Mech,.* Dec 1990, 57(4): 906-915

[16] J. Rivero, F. Vipiana, D. R. Wilton and W. A. Johnson, "Hybrid Integration Scheme for the Evaluation of Strongly Singular and Near-Singular Integrals in Surface Integral Equations," in *IEEE Transactions on Antennas and Propagation*, vol. 67, no. 10, pp. 6532-6540, Oct. 2019, doi: 10.1109/TAP.2019.2920333.

[17] A. A. Tambova, M. S. Litsarev, G. Guryev and A. G. Polimeridis, "On the Generalization of DIRECTFN for Singular Integrals Over Quadrilateral Patches," in IEEE Transactions on Antennas and Propagation, vol. 66, no. 1, pp. 304-314, Jan. 2018.

[18] A. G. Polimeridis, F. Vipiana, J. R. Mosig and D. R. Wilton, "DIRECTFN: Fully Numerical Algorithms for High Precision Computation of Singular Integrals in Galerkin SIE Methods," in IEEE Transactions on Antennas and Propagation, vol. 61, no. 6, pp. 3112-3122, June 2013.

[19] A. G. Polimeridis and J. R. Mosig, "On the Direct Evaluation of Surface Integral Equation Impedance Matrix Elements Involving Point Singularities," in IEEE Antennas and Wireless Propagation Letters, vol. 10, pp. 599-602, 2011.

[20] M. A. Khayat and D. R. Wilton, "Numerical evaluation of singular and near-singular potential integrals," IEEE Transactions on Antennas and Propagation, 53:3180–3190, 2007.

[21] S. M. Rao, D. R. Wilton, and A. W. Glisson, "Electromagnetic scattering by surfaces of arbitrary shape," *IEEE Trans. Antennas Propag.*, vol. AP-30, no. 3, pp. 409–418, May 1982.

[22] R. P. Bhatia and K. L. Lawrence, "Two-Dimensional Finite Element Mesh Generation Based on Stripwise Automatic Triangulation," in *Computers and Structures*, vol. 36, pp. 309–319, 1990.

[23] R. D. Graglia, D. R. Wilton and A. F. Peterson, "Higher order interpolatory vector bases for computational electromagnetics," in *IEEE Transactions on Antennas and Propagation*, vol. 45, no. 3, pp. 329-342, March 1997